Available online at www.sciencedirect.com

ScienceDirect

journal homepage: www.elsevier.com/locate/he

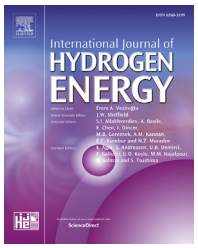

Au–Ni alloy nanoparticles supported on reduced graphene oxide as highly efficient electrocatalysts for hydrogen evolution and oxygen reduction reactions

Gitashree Darabdhara [a,b], Manash R. Das [a,b,*], Mohammed A. Amin [c,d,**], Gaber A.M. Mersal [c,e], Nasser Y. Mostafa [c,f], Sayed S. Abd El-Rehim [d], Sabine Szunerits [g], Rabah Boukherroub [g,***]

[a] Advanced Materials Group, Materials Sciences and Technology Division, CSIR-North East Institute of Science and Technology, Jorhat 785006, Assam, India
[b] Academy of Scientific and Innovative Research, CSIR-NEIST Campus, India
[c] Materials Science and Engineering Group, Department of Chemistry, Faculty of Science, Taif University, 888 Hawiya, Saudi Arabia
[d] Department of Chemistry, Faculty of Science, Ain Shams University, Abbassia 11566, Cairo, Egypt
[e] Department of Chemistry, Faculty of Science, South Valley University, Qena, Egypt
[f] Chemistry Department, Faculty of Science, Suez Canal University, Ismailia, Egypt
[g] Univ. Lille, CNRS, Centrale Lille, ISEN, Univ. Valenciennes, UMR 8520 - IEMN, Lille F-59000, France

ARTICLE INFO

Article history:
Received 11 September 2017
Received in revised form
21 October 2017
Accepted 6 November 2017
Available online 6 December 2017

Keywords:
Electrocatalysis
Au– Ni alloy nanoparticles
Reduced graphene oxide
Hydrogen evolution reaction
Oxygen reduction reaction
High stability

ABSTRACT

Bimetallic nanoparticles of Au and Ni in the form of alloy nanostructures with varying Ni content are synthesized on reduced graphene oxide (rGO) sheets *via* a simple solution chemistry route and tested as electrocatalysts towards the hydrogen evolution (HE) and oxygen reduction (OR) reactions using polarization and impedance studies. The Au–Ni alloy NPs/rGO nanocomposites display excellent electrocatalytic activity which is found to improve with increasing Ni content in the Au–Ni/rGO alloy nanocomposites. For HER, the best Au–Ni alloy NPs/rGO electrocatalyst, the one with the highest Ni content, exhibits high activity with an onset overpotential approaching zero *versus* the reversible hydrogen electrode and an overpotential of only 37 mV at 10 mA cm^{-2}. Additionally, a low Tafel slope of 33 mV dec^{-1} and a high exchange current density of 0.6 mA cm^{-2} are measured which are very close to those of commercial Pt/C catalyst. Also, in the ORR tests, this electrocatalyst displays comparable activity to Pt/C. The Koutecky–Levich plots referred to a 4-electron mechanism for the reduction of dissolved O_2 on the Au–Ni alloy NPs/rGO catalyst. The electrocatalyst thus demonstrates excellent activity towards HER and ORR.

* Corresponding author. Advanced Materials Group, Materials Sciences and Technology Division, CSIR-North East Institute of Science and Technology, Jorhat 785006, Assam, India.
** Corresponding author. Materials Science and Engineering Group, Department of Chemistry, Faculty of Science, Taif University, 888 Hawiya, Saudi Arabia.
*** Corresponding author.
E-mail addresses: mnshrdas@yahoo.com, mrdas@neist.res.in (M.R. Das), maaismail@yahoo.com (M.A. Amin), rabah.boukherroub@iemn.univ-lille1.fr (R. Boukherroub).
https://doi.org/10.1016/j.ijhydene.2017.11.048

Additionally, it exhibits outstanding operational durability and activation after 10,000th cycles assuring its practical applicability.

Introduction

Nourishing the ever increasing needs of the rapidly growing and developing modern society has created enormous demand for clean, renewable, environmentally friendly and affordable energy sources. In this context, exploitation of hydrogen (H_2) as a potential energy carrier, possessing the capability of replacing fossil fuels, has been a very attractive approach, primarily due to its large combustion heat (287 kJ/mol) and liberation of green by-product water [1]. A large fraction of hydrogen is generated from fossil resources *via* a steam reforming process that results in the production of H_2 along with CO_2, the latter is considered as a potential candidate for environmental global warming [2]. Thus, sustainable hydrogen generation *via* water electrolysis has proved to be one of the simplest, clean, renewable and large scale industrial methods [3]. Consisting of two half-cell reactions: hydrogen evolution reaction occurring at the cathode (HER i.e. $4H^+ + 4e^- \rightarrow 2H_2$) and oxygen evolution reaction occurring at the anode (OER i.e. $2H_2O \rightarrow O_2 + 4H^+ + 4e^-$), electrochemical water splitting demands advanced electrocatalysts that can reduce the overpotential and significantly improve the efficacy of the reaction [4]. Electrocatalysts for HER are classified as homogeneous and heterogeneous on the basis of the phase of reactants and the products. Widely used homogeneous HER catalysts include enzymes such as hydrogenases [5]. HER electrocatalysts are generally solids and their performance mainly depends on their surface properties [6]. The ease of separation makes the heterogeneous HER electrocatalysts attractive candidates.

Because of its non-zero overpotential, Pt (Pt/C) is in depth explored for both HER and ORR, even though Pt is restricted for commercial applications because of its rare and expensive nature [7]. The reaction rate at the cathode for HER using Pt catalyst is extremely fast whereas the anodic reaction is sluggish and necessitates higher Pt loading. It is hence extremely important and challenging to design highly operative, cost effective and stable electrocatalysts for HER and ORR.

To tackle this problem, researchers have developed engineered nanostructures of different Pt group metals (Ru, Rh, Ir, Pd) possessing high surface to volume ratio for achieving high electrochemical performances [8]. Monolayer Pt supported on bulk tungsten carbide (WC) [9], Pt nanoparticles (NPs) supported on TiO_2, nitrogen-doped reduced graphene oxide (rGO) based Pt–TiO_2 nanostructures [10], monolayer Pd and Au supported on Mo_2C [11] etc. were used as HER electrocatalysts exhibiting excellent activity. Nanoscale Au-based nanocomposites such as graphene quantum dots/Au hybrid NPs [12], Au/carbon nanotubes, Au/graphene nanocomposites [13], Au NPs supported on multi-walled carbon nanotubes [14], Au NPs supported on rGO [15] etc. have also been explored as effective HER electrocatalysts. Similarly, efforts to avoid the use of precious Pt metal in ORR have led to the use of Au NPs supported on reduced graphene oxide [16], Pd NPs on different supports such as Pd/Vulcan [17], Pd on multi-walled carbon nanotubes [18], Pd on nitrogen-doped graphene [19], alloyed Pd-Ag [20], polymer based hybrid catalyst with low Pt content [21], etc.

Efforts to circumvent the use of precious noble metals have led to an extensive research for alternate non-noble (Fe, Co, Ni, Mo) and metal-free (carbon based) electrocatalysts [22–24]]. Other non-noble electrocatalysts include transition metal chalcogenides [25], carbides [26], metal alloys [27] and complexes [28]. Consisting of two elements, bimetallic NPs in either alloys or core-shell nanostructures have gained immense interest as effective HER and ORR electrocatalysts as well as in different energy storage applications [29–32]. This is mainly due to their enhanced and tuneable chemical and physical properties along with cooperative interactions which contribute to their superior catalytic properties in comparison to their monometallic counterparts [6]. Alloying two different metals allows to increase the specific surface sites and also to decrease the amount of catalyst loading, leading to enhanced HER and ORR [33]. Amongst bimetallic alloys, Au–Pd acts as an ideal electrocatalyst towards HER [34,35]. Alloy nanostructures based on Cu-Pt [36], Au-Pt [37] etc. exhibit excellent HER activity. Core-shell nanostructures also possess the capacity of replacing Pt in several HER reactions. For instance, Au@Pt [38], Cu@Pd/Ti [39], Au@Pd [40], Au@CdS core–shell nanostructures [41] etc. have shown excellent performances.

Because of the high abundance, catalytic nature and low cost, Ni is chosen as a good candidate from the non-noble elements for HER as well as ORR. However, the relatively high affinity of Ni for hydrogen attributes to the difficulty in hydrogen desorption. Additionally, Ni is prone to corrosion in acidic media upon continuous electrolysis [42]. Thus, far-reaching efforts have been dedicated towards alloying Ni with other elements for constructing active and durable electrocatalysts. A large number of Ni-based alloys like Ni-Sn [43], Ni-Mo [44], Ni-Fe [45], Ni-Se [46], etc. have been identified in electrochemical conversion of H_2O to H_2. Alloyed Ni-Mo [47], CoNi/ultrathin graphene layer [48] and core shell IrNi-nitride NPs [49], Pt@Ni_3/C [50], Ni@Pd-polyethyleneimine-rGO [51], etc. acted as active Ni containing bimetallics towards effective HER.

Another major influencing factor in electrocatalytic efficiency remains the conducting property of the electrocatalyst. A large number of carbon-based materials like carbon black, carbon nanotubes, or graphene supports for the synthesis of NPs as well as improving electrocatalytic activity have aroused [4]. Among them, the 2D wonder material "graphene" has received widespread attention. Graphene oxide (GO) and rGO have emerged as excellent supports for NPs' synthesis, yielding nanocomposites with high potential for a myriad of applications [52]. Theoretically, interaction between metal and graphene leads to changes in the Fermi level of both

materials, leading to their enriched catalytic activity [53]. Thus, designing GO- and rGO-based materials with excellent catalytic applications is of great interest.

Taking into account the importance of graphene-based bimetallic NPs as well as activity of both individual Au and Ni for HER and ORR, we attempted to combine Au and Ni of different Au/Ni ratios on rGO to form Au–Ni alloy NPs/rGO nanocomposites using an easy and a simple solution chemistry reduction method. The nanocomposites have been characterized by high resolution transmission electron microscopy (HRTEM), X-ray diffraction (XRD), X-ray photoelectron spectroscopy (XPS), thermal gravimetric analysis (TGA), and diffuse reflectance infrared Fourier transform (DRIFT) spectroscopy. The developed nanocomposite materials have been investigated for the first time as electrocatalysts towards HER and ORR, employing various electrochemical techniques. The best Au–Ni alloy NPs/rGO catalyst exhibited high HER activity with an onset overpotential approaching zero versus the reversible hydrogen electrode (RHE) and an overpotential of only 37 mV at 10 mA cm^{-2}. Additionally, a low Tafel slope of 33 mV dec^{-1} and a high exchange current density of 0.6 mA cm^{-2} were recorded. These electrochemical HER parameters are very close to those of commercial Pt/C catalyst with outstanding operational durability and activation after 10,000th cycles. Also, in the ORR tests, this catalyst exhibited comparable activity to Pt/C with a 4-electron mechanism for the reduction of dissolved O_2.

Experimental

Chemicals and reagents

Graphite powder (<20 μm, Sigma-Aldrich), sulfuric acid (Qualigens), hydrochloric acid (Qualigens), hydrogen peroxide (Qualigens), potassium permanganate (Merck), gold (III) chloride trihydrate (>99.9%, Sigma Aldrich), nickel (II) chloride (>99.9%, Alfa Aesar), hydrazine hydrate (Sigma Aldrich), and sodium hydroxide (Qualigens) were used as received.

Preparation of electrocatalysts

GO was synthesized by the Hummers and Offeman method in which graphite powder (2 g) was oxidized in the presence of $KMnO_4$ (6 g) and H_2SO_4 (46 mL) followed by exfoliation under high power ultrasonication (using SONICS Vibra cell ultrasonicator operating at a frequency of 20 KHz ± 50 Hz) for 1 h to obtain a homogeneous GO suspension [54]. A GO suspension (10 mg/mL) was used to synthesize rGO modified with Au–Ni alloy NPs, yielding Au–Ni alloy NPs/rGO composites. The nanocomposites were synthesized using different concentrations of Ni. Typically, to an aqueous solution of 3, 5 or 10 mM $NiCl_2$, $HAuCl_4$ solution (3 mM) was added and allowed to stir for 20 min followed by the addition of 15 mL of GO solution (10 mg/mL). To this solution, hydrazine hydrate (3.2 M) was added slowly and then heated to 75 °C for 15 min. The total volume of the entire reaction mixture was maintained at 40 mL. Finally, 40 mg of NaOH was added and left to stir for 3 h at 80 °C to obtain a black solution. The solution was filtered and dried in an air oven at a temperature of 65 °C to obtain a solid black catalyst. Basic medium (i.e. in presence of NaOH) is favorable for easy decomposition of the reducing species N_2H_4: $N_2H_4 + 4OH^- = N_2 + 4H_2O + 4e^-$. These electrons participate in the reduction of the metal salts to their corresponding nanoparticles during the synthesis.

Monometallic Au/rGO and Ni/rGO were prepared adopting similar procedure by mixing GO suspension with either aqueous $HAuCl_4$ or $NiCl_2$ solution. All other reaction conditions were kept similar to that required for the synthesis of bimetallic Au–Ni/rGO nanocomposites.

Characterization

The X-ray diffraction (XRD) patterns were obtained using a Rigaku X-ray diffractometer (model: ULTIMA IV, Rigaku, Japan) at a scanning rate of 3°/min. The instrument uses Cu Kα (λ = 1.54056 Å) as the X-ray source and operates at a generator voltage of 40 kV and a generator current of 40 mA. All the XRD patterns were recorded in the 2θ value ranging from 5 to 80°.

The shape, size, morphology and the crystal structure of the nanocomposites were determined using transmission electron microscope (TEM) and high-resolution TEM (HRTEM), model-JEOL JEM 2100, Japan, operating at an accelerating voltage of 200 kV. For recording the TEM micrographs, standard carbon-coated copper grids were used onto which dispersed colloidal solutions of the prepared nanocomposites in water were dropped, followed by air drying at room temperature.

X-ray photoelectron spectroscopy (XPS) measurements were carried out using an ESCALAB 220 XL spectrometer having a monochromatic Al Kα X-ray source (1486.6 eV) and a spherical energy analyzer that operates in the CAE (constant analyzer energy) mode using the electromagnetic lens mode. The CAE for survey spectra is 100 eV and that for high-resolution spectra is 40 eV. The angle between the incident X-rays and the analyzer is 58°. The detection angle of the photoelectrons is 30°.

Thermal analysis (TGA) of the nanocomposite samples was carried out using a Thermal Analyzer (Model: Netzsch STA 449F3). For TGA analyses, approximately 10 mg of each sample were taken in the crucible and heated from 20 to 1000 °C at a heating rate of 10 °C/min in a nitrogen environment.

Diffuse reflectance infrared Fourier transform (DRIFT) spectra were recorded in transmittance mode at 4 cm^{-1} spectral resolution in the 400–4000 cm^{-1} range using an IR Affinity-1 FTIR spectrophotometer (Shimadzu, Japan) furnished with a DRS-8000 DRIFT accessory.

Specific surface area of the samples was recorded at 77 K *via* nitrogen gas adsorption by applying Brunauer–Emmett–Teller (BET) calculations and using an Autosorb-iQ Station 1 (Quantachrome, USA). The samples were previously degassed at 200 °C for 3 h before performing the experiment.

The metal content and the atomic ratio of Au:Ni was calculated using a flame Atomic Absorption Spectrophotometer (Perkin Elmer, Analyst 200).

Electrochemical measurements

Electrochemical characterizations towards HER and ORR were carried out in a standard three-electrode electrochemical cell,

in which glassy carbon (GC, 3 mm) with various catalysts, saturated calomel, and graphite rod (Sigma-Aldrich, 99.999%) were used as the working, reference and auxiliary electrodes, respectively. All electrochemical measurements were conducted without iR compensation, as the test solution is highly conductive and the cell geometry is ideal, where the reference electrode was inserted into a Luggin capillary filled with the test solution, too. The tip of the Luggin capillary was placed as close as possible to the working electrode to achieve maximum reduction in iR drop in electrolytes. In addition, polarization curves without and with iR compensation were found to be almost the same (see representative examples on Fig. S1, Supporting Information).

All potentials were measured against saturated calomel electrode (SCE) and calibrated here to the reversible hydrogen electrode (RHE) scale by adding a value of $(0.241 + 0.059 \times pH)$ V. Various electrochemical techniques were applied to the GC-loaded catalyst/H_2SO_4 interfaces by connecting the cell to an Autolab, PGSTAT30/FRA system (Ecochemie, The Netherlands). Measurements were conducted in 200 mL deaerated and O_2-saturated aqueous solutions of H_2SO_4 (0.5 M). Temperature of the solution was maintained at $(25 \pm 0.2\ ^\circ C)$ using a temperature-controlled water bath.

The GC working electrode was first polished with alumina powder of 0.3 μm followed by 0.05 μm till a mirror-like surface was obtained. Then it was ultrasonically washed with doubly distilled-water for at least 20 min, and finally dried in air. The GC-loaded catalyst working electrode was prepared as follows. The catalyst ink was first prepared *via* ultrasonic dispersion of the catalyst powder in distilled water (Milli-Q) containing 0.5 wt % of Nafion. Then, an aqueous dispersion of the catalyst (20 μL, 1.0 mg/mL) was dropped onto the freshly polished GC electrode. The amount of the catalysts was about 25 μg cm^{-2}. The working electrode was then inserted in a rotating disc system developed by Ω Metrohm Autolab B.V. (Serial no: RDE80526) for electrochemical measurements.

Linear sweep voltammetry (LSV) was conducted at a scan rate of 5 mV s^{-1} in deaerated and O_2–saturated 0.5 M H_2SO_4 aqueous solutions to assess the activity of our synthesized catalysts towards the HER and ORR. Electrochemical impedance spectroscopy (EIS) measurements were carried out using working electrode biased at a cathodic overpotential of −0.35 V *vs.* RHE, and superimposing a small sinusoidal voltage of 5 mV in the frequency range of 100 kHz to 10 mHz. The experimental data were fitted to an appropriate equivalent circuit model using the complex nonlinear least-squares method.

HER Faradaic efficiencies for the studied catalysts were determined by quantifying the amount of H_2 generated during controlled potential electrolysis by gas chromatography, and dividing that by the amount of H_2 expected based on the charge passed (assuming 100% Faradaic efficiency) through the working electrode (*WE*) during that electrolysis. Measurements were conducted in a custom-made air-tight electrolysis cell containing 0.5 M H_2SO_4 solution by holding the electrode at −0.85 V *vs* RHE for 1 h. Gas chromatography was conducted on an Agilent 7890A gas chromatograph with a pneumatically operated automatic gas sampling valve to monitor the evolved H_2 gas. The electrolysis cell was connected to the gas chromatography system *via* bespoke air-tight glass-to-metal adapters and copper tubing with internal diameter of 1/8 inch. The oven temperature was set to 45 °C and the carrier gas was Ar at a flow rate of approximately 3 mL min^{-1}.

The durability and stability of the most active catalyst was evaluated by 24 h of chronoamperometry measurements at a fixed cathodic overpotential and continuous potential cycling up to 10,000 cycles. Each run was repeated at least 3 times to confirm reproducibility of the results. The reported data are found to be statistically significant; their arithmetic mean and standard deviation were calculated and reported.

Results and discussion

Characterization of Au–Ni/rGO, Au/rGO, and Ni/rGO nanocomposite materials

All the XRD patterns of Au–Ni/rGO nanocomposites with various Ni contents prepared using different concentration of Ni salt namely Au–Ni 1/rGO (Au = 3 mM and Ni = 3 mM), Au–Ni 2/rGO (Au = 3 mM and Ni = 5 mM), Au–Ni 3/rGO (Au = 3 mM and Ni = 10 mM) and monometallic Au/rGO and Ni/rGO nanocomposites are presented in Fig. 1. The diffraction peaks of Au/rGO at 2θ values of 38.06°, 44.28°, 64.58° and 77.58° correspond to Au(111), Au(200), Au(220) and Au(222) planes, respectively (JCPDS: 01-071-3755). Also, the diffractions of Ni/rGO occur at 2θ values of 44.38°, 51.72° and 76.28° corresponding to Ni(111), Ni(200) and Ni(220) planes, respectively (JCPDS: 00-004-0850). Compared with the peaks of pure Au NPs, the diffraction peaks of Au–Ni/rGO nanocomposites shift slightly to higher 2θ values thus confirming that Ni has entered into the Au lattice forming Au–Ni alloy form. A similar observation has been reported by Chen et al. for Ni–Au NPs [55,56]. Similarly, they also found that the characteristic peaks for the alloyed Ni–Au NPs were slightly broader than those of individual Au as also obtained in our case, suggesting lowered crystallinity of the alloy [57]. For the Au–Ni 1/rGO and Au–Ni 2/rGO nanocomposites, the characteristic peaks of Ni(111) and Ni(220) at 44.38° and 76.28° overlapped with those of (200) and (311) planes of Au at 2θ values of 44.28° and 77.58°.

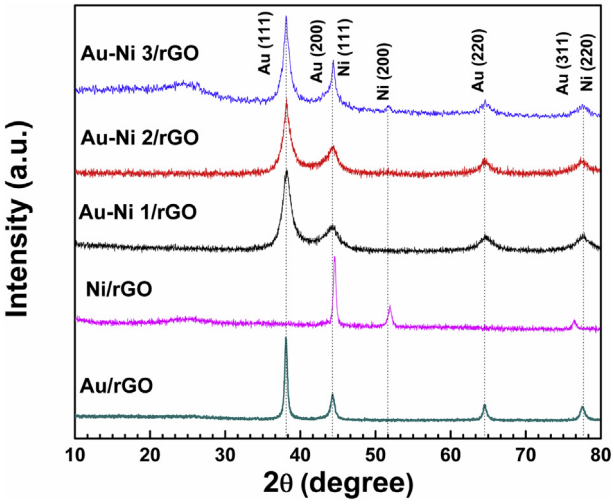

Fig. 1 – XRD patterns of monometallic Au/rGO, Ni/rGO and Au–Ni/rGO nanocomposites.

For Au–Ni 1/rGO, diffraction peaks were observed at 38.16° for Au(111), 44.34° for Au(200) and Ni(111), 64.74° for Au(220) and 77.62° for Au(222) and Ni(220). For Au–Ni 2/rGO, diffraction peaks appeared at 38.16°, 44.36°, 64.46° and 77.56° 2θ value. The (111) and (200) peaks of the synthesized Au–Ni/rGO nanocomposites lie between those of individual Au and Ni NPs, suggesting the formation of *fcc* Au–Ni alloy. However, for Au–Ni 3/rGO, although diffractions appeared at similar 2θ values as those of Au–Ni 1/rGO and Au–Ni 2/rGO, an additional weak diffraction at 2θ value of 51.7° was observed, corresponding to Ni(200). The intensity of the diffraction peak at 51.7° was distinct for Au–Ni 3/rGO. The presence of this diffraction peak with increasing Ni concentration in Au–Ni 3/rGO indicated the presence of weak *fcc* Ni-phase [58]. In accordance with Vegard's law which states that the diffraction peak of a metal alloy lies between the two set peaks of pure metals, the diffraction peaks for our synthesized Au–Ni nanoparticles lie between the diffraction peaks of pure Au and Ni nanoparticles thus confirming the possible formation of metal alloy [56].

Furthermore, the peak of GO at 2θ value of 11.7° was not observed in any of the synthesized nanocomposites and the presence of a broad peak ~24.5° confirmed the simultaneous reduction of GO to rGO during NP formation using hydrazine hydrate. However, due to the strong diffraction peaks from the bimetallic Au–Ni alloy as well as from the monometallic Au and Ni, the diffraction, peaks from rGO might be shielded due to the high quantity of NPs in the Au–Ni/rGO nanocomposite. We have reported similar observations in our previous publications [59,60].

The morphology, size, shape, crystallinity and distribution of the Au–Ni alloy NPs on rGO sheets were investigated by TEM and HRTEM analysis. Typical TEM and HRTEM images of different Au–Ni/rGO nanocomposites are displayed in Fig. 2. The TEM images of Au–Ni 1/rGO show the formation of well dispersed and spherical shaped NPs distributed over the folded and wrinkled sheets of rGO with an average size diameter of around 14.5 ± 0.1 nm, calculated using Image J software (Fig. 2c). The selected area electron diffraction (SAED) pattern (Fig. 2a (inset)) depicts several bright spots which reflect the polycrystalline nature of the Au–Ni 1/rGO nanocomposite. The HRTEM image validates the crystallinity as well as alloy nature of the Au–Ni 1/rGO nanocomposite. The HRTEM image in Fig. 2b exhibits clear lattice fringes that can be indexed to *fcc* Au (111) plane with an interplanar spacing of 0.230 nm and to *fcc* Ni (111) plane with an interplanar spacing of 0.203 nm. The presence of clear lattice fringes indicates a random mixture of both metals in one particle. Similar TEM and HRTEM images were recorded for Au–Ni 2/rGO with a size distribution of 17.2 ± 0.3 nm (Fig. 2d–f). The SAED pattern (Fig. 2d (inset)) and the HRTEM image confirm the crystalline nature of the nanocomposite. Here also clear lattice fringes corresponding to both Au (111) and Ni (111) with lattice fringes of 0.230 and 0.203 nm are clearly observed, confirming the presence of both metals in the form of bimetallic alloy structure. For Au–Ni 3/rGO, the TEM image (Fig. 2g) shows the formation of polydisperse NPs of Au–Ni with an average size diameter of 16 ± 0.2 nm (Fig. 2i). The SAED pattern (Fig. 2g (inset)) along with the HRTEM (Fig. 2h) image reveal the crystalline nature of the nanocomposite. The HRTEM image confirms the bimetallic nature of the nanocomposite with clear lattice fringes of both Au (111) and Ni (111) plane with interplanar spacing of 0.230 and 0.203 nm, respectively. The HRTEM image of Au–Ni 3/rGO nanocomposite also indicates a random mixture of both metals in one particle, confirming the alloy nature of the nanostructures. As the content of Ni in the Au–Ni gradually increases in the Au–Ni/rGO nanocomposites, the NPs tend to be more polydisperse in nature and with further increase in concentration the NPs tend to agglomerate. Nanoparticles' aggregation will decrease the surface active sites on the nanocomposites and consequently their catalytic efficiency decreases. Additionally, the TEM images show the presence of wrinkled and folded rGO sheets thus confirming the formation of the bimetallic nanocomposites on their surface.

For comparison, TEM and HRTEM images along with size distribution histograms of monometallic Au/rGO and Ni/rGO are displayed and discussed in Fig. S2 (Supporting Information).

Thermal stability of the Au–Ni alloy/rGO nanocomposites was ascertained from the TGA analysis carried out under N_2 atmosphere (Supporting Information, Fig. S3A). For comparison, the TGA plots of Au/rGO and Ni/rGO are shown in Supporting Information, Fig. S3B. They indicate major weight losses at 100 °C and 200 °C, and a slight loss above 500 °C. Loss of water molecules that are present in between the layers of graphene can be observed at 100 °C. The weight loss above 200 °C is due most likely to removal of residual oxygen-containing functional groups, like carboxyl, carbonyl, hydroxyl, and epoxy groups on the surface of rGO. The weight loss above 500 °C is attributed to the loss of carbon skeleton of the rGO sheets. For comparison, readers may refer to the TGA curves of GO and rGO in our previous publication [61].

The presence of different functional groups on the nanocomposites was further demonstrated using DRIFT spectroscopy (Supporting Information, Fig. S4). For all the nanocomposites, the DRIFT stretching frequencies corresponding to the different functional groups on rGO surface are summarized in Table S1. It can be seen that compared to GO (which is discussed elsewhere [62], the stretching of oxygen functionalities like O–H and C=O groups are greatly reduced, indicating successful conversion of GO to rGO during nanocomposite formation.

The BET surface area of all the Au–Ni/rGO nanocomposites and that of the monometallic Au/rGO and Ni/rGO are provided in Table 1. As compared to support rGO, the surface area of all rGO based monometallic/bimetallic nanocomposites is quite high. Monometallic Au/rGO has a surface area of 44.98 m^2/g, whereas Ni/rGO possesses the highest BET surface area of 268.29 m^2/g probably due to its smallest size (~6 nm). All the bimetallic nanocomposites exhibit an average surface area above 230 m^2/g with highest value for Au–Ni 3/rGO nanocomposite (240.05 m^2/g), which is in fact the most active catalyst among all synthesized nanocomposites.

The chemical composition of the different Au–Ni/rGO nanocomposites was examined using XPS (Fig. 3, Table 2). For comparison XPS results of the monometallic composites, Au/rGO and Ni/rGO, prepared under otherwise identical conditions, are provided. The XPS survey spectrum of Au–Ni 3/rGO nanocomposite is displayed in Fig. 3A. It exhibits peaks

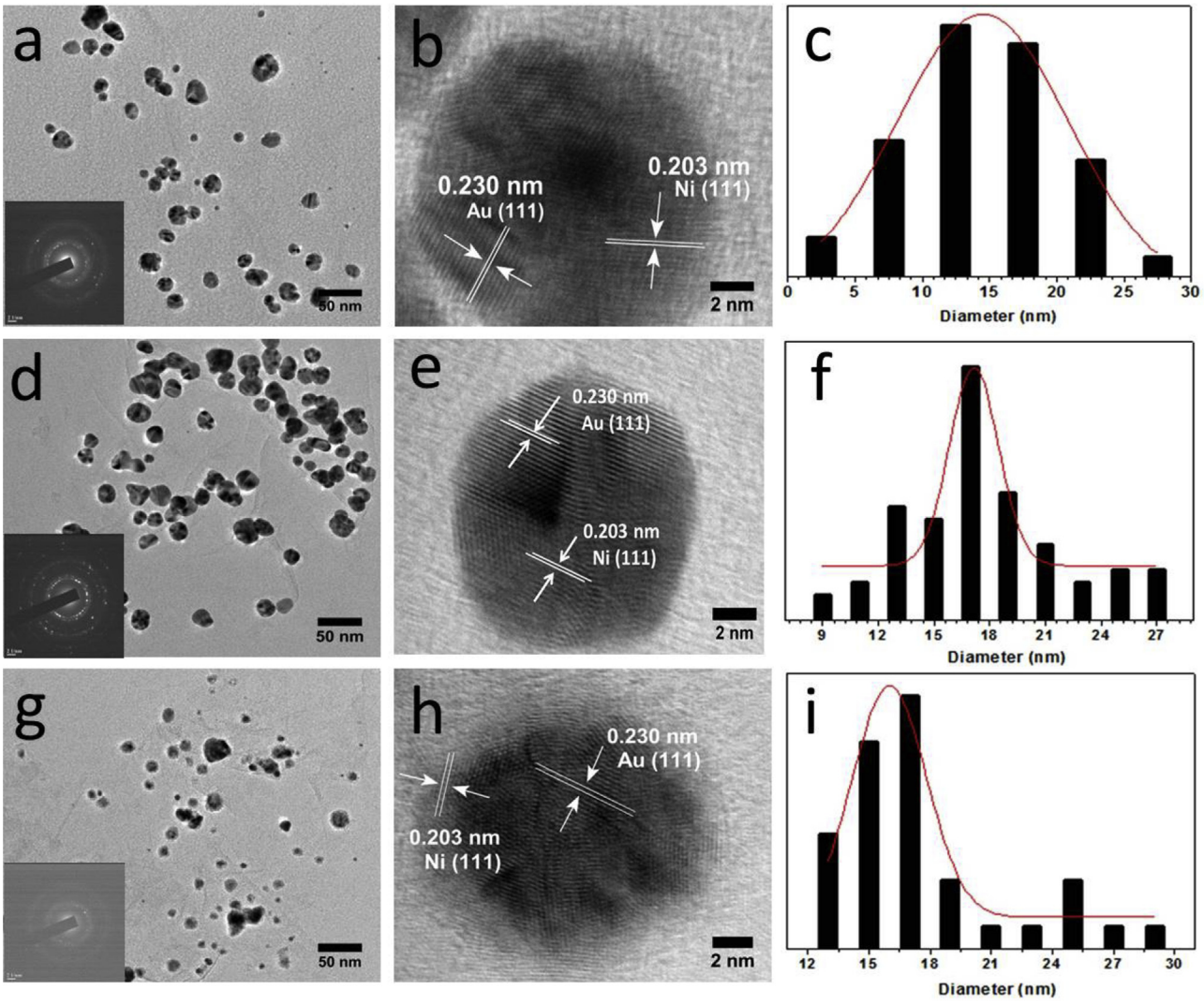

Fig. 2 – TEM images (a, d, g); HRTEM images (b, e, h), and size distribution histograms (c, f, i) of Au–Ni 1/rGO, Au–Ni 2/rGO and Au–Ni 3/rGO nanocomposites, respectively. The insets in (a, d, g) correspond to the SAED patterns for Au–Ni 1/rGO, Au–Ni 2/rGO and Au–Ni 3/rGO nanocomposites, respectively.

Table 1 – BET surface area of Au–Ni/rGO, Au/rGO and Ni/rGO nanocomposites.

Material	Surface area (m^2/g)
Au–Ni 1/rGO	234.02
Au–Ni 2/rGO	233.47
Au–Ni 3/rGO	240.05
Au–Ni 3/rGO after cathodic activation[a]	624.49
Au/rGO	44.98
Ni/rGO	268.29
rGO	37.02
rGO after cathodic activation[a]	108.07

[a] Repetitive cycling (10,000 cycles) between E_{corr} and −0.2 V(RHE) at a scan rate of 100 mV s^{-1} in 0.5 M H_2SO_4 solution at 25 °C.

corresponding to C_{1s} (284.4 eV), O_{1s} (532.6 eV), Au_{4f} (84.0 eV), and Ni_{2p} (856.1eV). Representative Au_{4f}, Ni_{2p} and C_{1s} high resolution XPS spectra are depicted in Fig. 3B–D. The Au_{4f} high resolution XPS spectrum of Au–Ni 3/rGO displays two peaks corresponding to $Au_{4f7/2}$ and $Au_{4f5/2}$ at 84.0 and 87.6 eV, respectively (Fig. 3B), consistent with Au metal in zero valence state. The Ni_{2p} high resolution XPS spectrum displays two major peaks centered at 856.1 and 873.6 eV with a spin-energy separation of 17.5 eV due to $Ni_{2p3/2}$ and $Ni_{2p1/2}$, respectively (Fig. 3C). These bands are characteristic of $Ni(OH)_2$ phase, in agreement with other literature reports [63–65]. The two extra peaks centered at 861.1 and 879.5 eV correspond to $Ni_{2p3/2}$ and $Ni_{2p1/2}$ satellite peaks, respectively. Fig. 3D depicts the C_{1s} high resolution spectrum of Au–Ni 3/rGO. It can be deconvoluted into four components with binding energies at about 283.8, 284.5, 287.3 and 289.2 eV assigned to C=C (sp^2 network), C–C/C–H, C=O and HO–C=O species, respectively. The C/O ratio varies significantly depending on the initial Au/Ni ratio used for the synthesis of Au–Ni/rGO (Table 2). Decreasing the Au^{3+}/Ni^{2+} ratio leads to a decrease in the atomic percentage of Au_{4f} in the nanocomposite material. Surprisingly, the same trend was observed for Ni.

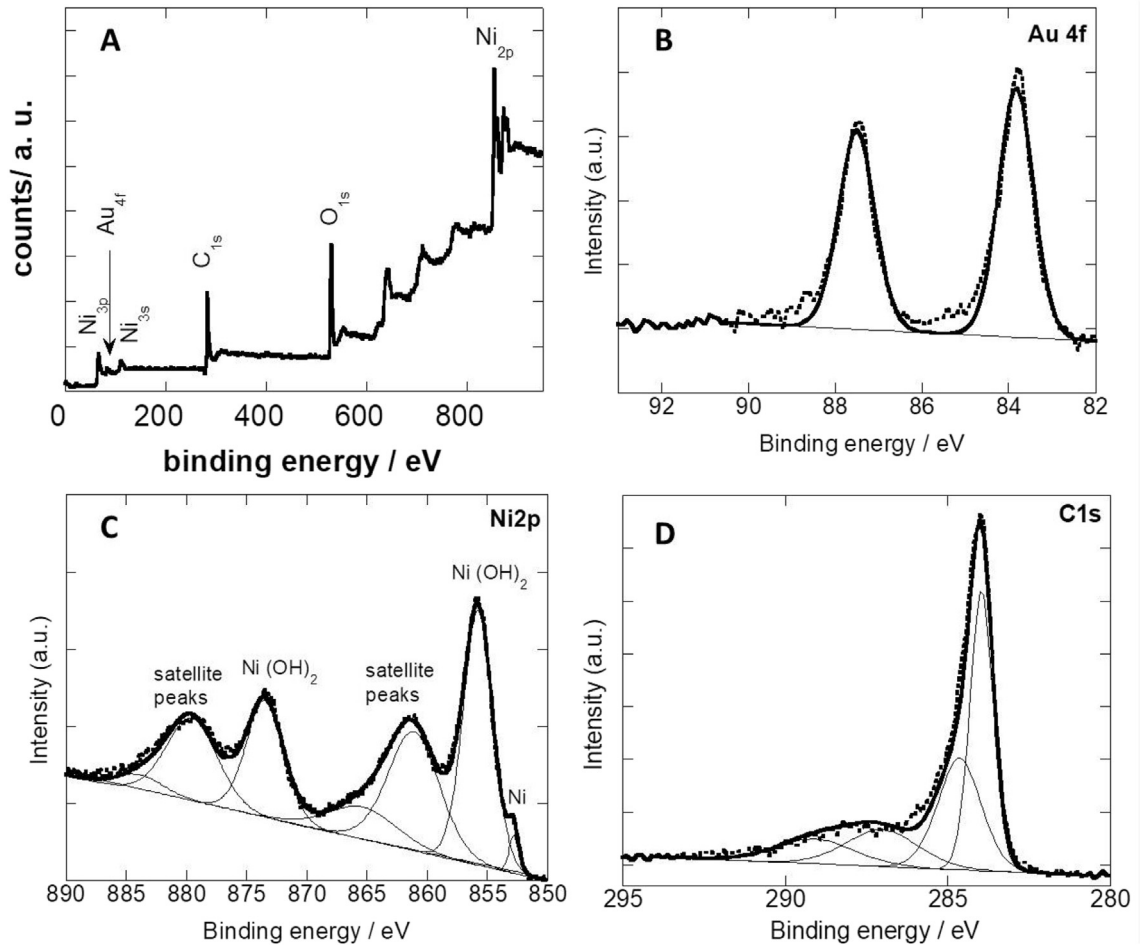

Fig. 3 – XPS survey spectrum (A); High resolution XPS spectra of Au_{4f} (B); Ni_{2p} (C) and C_{1s} (D) of Au–Ni 3/rGO nanocomposite.

Table 2 – Chemical composition (at.%) determined by XPS.

Material	C_{1s}	O_{1s}	Ni_{2p}	Au_{4f}	C/O
Au–Ni 3/rGO	43.8	34.2	19.1	2.9	1.28
Au–Ni 2/rGO	51.9	30.8	16.1	1.2	1.68
Au–Ni 1/rGO	81.7	12.7	4.8	0.8	6.44
Au NPs/rGO	91.3	7.9	–	0.8	11.5
Ni NPs/rGO	84.9	13.5	1.6	–	6.2

The AAS technique also confirms the presence of both Au and Ni in the Au–Ni/rGO nanocomposites and their contents are provided in Table S2 in the SI.

Electrochemical measurements

Catalytic activity for the HER

Fig. 4a displays the HER performance of the Au–Ni NPs/rGO (curves 4–6) in comparison with bare rGO (curve 1), Au NPs/rGO (curve 2), Ni NPs/rGO (curve 3), and Pt/C (curve 7). All measurements were carried out in 0.5 M H_2SO_4 deaerated solution at a scan rate of 5.0 mV s^{-1} at 25 °C. The onset potential for the HER, E_{HER}, needed for the Pt/C catalyst is close to zero *vs.* RHE, demonstrating its well-known superior HER catalytic activity. By contrast, bare rGO showed a larger E_{HER} (−344 mV *vs.* RHE) accompanied by much smaller reduction currents for the HER, thus exhibiting poor activity for the HER. The HER activity of the studied electrocatalysts, particularly the three synthesized Au–Ni alloy NPs/rGO catalysts (Fig. 4a: curves 4–6), come far beyond that of the bare rGO, approaching that of Pt/C. This is clear from their measured E_{HER} values (Table 3), where E_{HER} value of Ni NPs/rGO catalyst (−126 mV *vs.* RHE) is 59 mV more positive than that recorded for Au NPs/rGO catalyst (−185 mV *vs.* RHE), demonstrating the high catalytic performance of the former. The relatively smaller size of the Ni NPs loaded on rGO, along with the high specific surface area of the Ni NPs/rGO catalyst (6 nm and 268.39 m^2/g, respectively), are the main reasons behind the higher HER activity of such catalyst as compared to Au NPs/rGO catalyst (13 nm and 44.98 m^2/g, respectively). Au NPs/rGO catalyst in turn is anodic to bare rGO by 159 mV *vs.* RHE. Table 3 also reveals that the values of E_{HER} measured for any of the synthesized Au–Ni NPs/rGO catalysts are more positive than that of the Ni NPs/rGO catalyst. These findings mean that the kinetics of the HER gets quicker when the NPs of both Au and Ni are brought together on rGO as bimetallic (curves 4–6) rather than loaded individually (curves 2 and 3). Similar results were previously obtained for supported bimetallic NPs of Au-Pd [34,66], Cu-Ti [67] as electrocatalysts for the HER. The

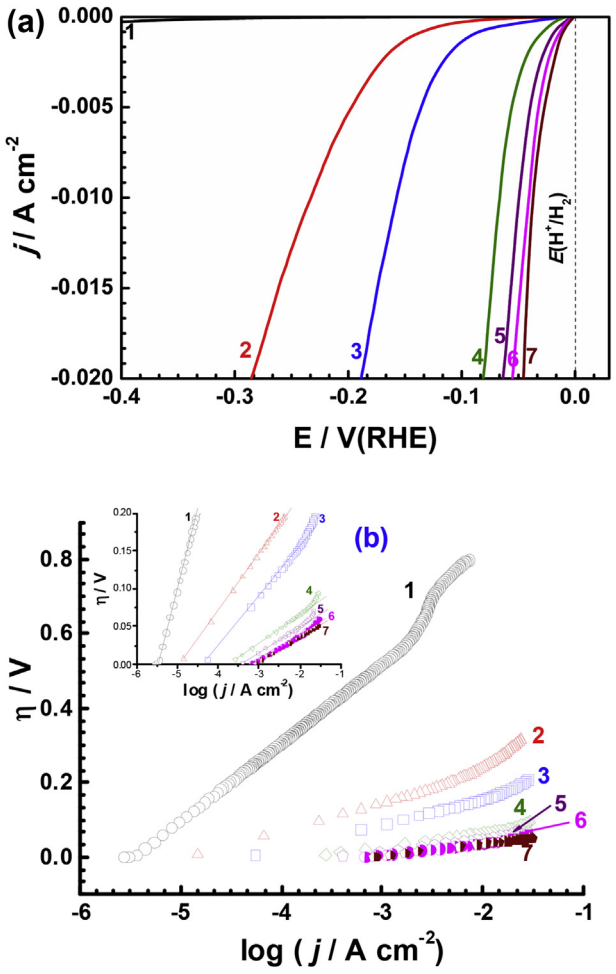

Fig. 4 – (a) Polarization curves and (b) corresponding Tafel plots of the synthesized electrocatalysts loaded onto a glassy carbon electrode (rotation speed 1600 rpm). Measurements were conducted in deaerated H_2SO_4 aqueous solution (0.5 M) at a scan rate of 5 mV s^{-1} at 25 °C: (1) bare rGO; (2) Au NPs/rGO; (3) Ni NPs/rGO; (4) Au–Ni 1/rGO; (5) Au–Ni 2/rGO; (6) Au–Ni 3/rGO; (7) Pt/C.

improved HER catalytic performance of the Au–Ni NPs/rGO catalyst can be credited to the synergistic effect occurring between Au and Ni [34,36,66,67]. Such cooperative influence enhances with increasing the Ni concentration in the Au–Ni alloy/rGO catalyst. This is clear from the values of E_{HER} measured for our synthesized Au–Ni/rGO catalysts. As shown in Table 3, the E_{HER} values needed for Au–Ni 1/rGO, Au–Ni 2/rGO, and Au–Ni 3/rGO catalysts are −50, −25, and −7 mV *vs.* RHE, respectively. It is worth mentioning that for Ni NPs/rGO (Fig. 4a, curve 3), the catalyst with the least average particle size for the loaded NPs and the highest specific surface area among the tested catalysts (Table 1), exhibited HER activity much lower than any of the studied Au–Ni NPs/rGO catalysts (Fig. 4a, curves 4–6). These findings suggest that the cooperative catalytic influence between Au and Ni is the most important parameter for the outstanding HER catalytic performance of the Au–Ni alloy NPs/rGO catalysts.

The above findings reflect the high catalytic performance of our catalysts, which originate from the synergetic chemical coupling effects between the loaded metal NPs and the rGO which allows the growth of highly dispersed metal NPs on the rGO surface selectively. Such dispersed metal NPs could serve as active catalytic sites for the HER. In addition, the substrate used here provides a large surface area (37.02 m^2/g), based on the Brunauer–Emmett–Teller (BET) analysis in Table 1, for better dispersion of the supported NPs. This in turn results in high contact area thus, facilitating H^+ reduction *via* the exposure of more active sites.

Kinetics of the HER

The HER kinetics over such catalysts was investigated by the corresponding Tafel plots, Fig. 4b. Tafel slope (β_c) and exchange current densities (j_o) were calculated by means of the least-square analysis of the Tafel plots. The fitting parameters are also shown in Table 3. The values of j_o measured for these catalysts were used to evaluate their HER inherent activity. Au–Ni/rGO catalysts recorded the highest j_o values (0.18, 0.35, and 0.6 mA cm^{-2} for Au–Ni (1, 2, and 3)/rGO, respectively) among the studied materials (3.2×10^{-3}, 1.3×10^{-2}, and 4.1×10^{-2} mA cm^{-2} for bare rGO, Au NPs/rGO and Ni NPs/rGO, respectively). These results support the superior HER kinetics of Au–Ni/rGO catalysts. The j_o of 0.6 mA cm^{-2} for the most active catalyst, Au–Ni 3/rGO, is very close to that of Pt/C catalyst (0.8 mA cm^{-2}) and also outperforms that of most reported HER catalysts (Supplementary Table S3).

In addition, in order to attain a high current density of 10 mA cm^{-2}, the Au–Ni (1, 2, and 3)/rGO catalysts only require overpotentials of about 70, 50, and 40 mV, respectively. However, the overpotentials needed for their corresponding individual catalysts, namely Au NPs/rGO and Ni NPs/rGO are about 222 and 158 mV, respectively. These results again

Table 3 – Mean value (standard deviation) of the electrochemical kinetic parameters for the HER on the surfaces of the synthesized electrocatalysts in deaerated 0.5 M H_2SO_4 solution at 25 °C, in comparison with those recorded for bare rGO and Pt/C.

Tested cathode	Onset potential (E_{HER}, mV *vs.* RHE)	Tafel slope (mV dec^{-1})	Exchange current density (j_o, mA cm^{-2})	Overpotential at j = 10 mA cm^{-2} (η_{10}, mV)
bare rGO	−344(7)	−211(3)	$3.2(0.05) \times 10^{-3}$	
Au NPs/rGO	−185(4.8)	−77(2.2)	$1.3(0.02) \times 10^{-2}$	220(5)
Ni NPs/rGO	−126(4.2)	−66(2)	$4.1(0.03) \times 10^{-2}$	158(2.4)
Au–Ni 1/rGO	−50(3)	−40(1.9)	0.18(0.01)	70(1.6)
Au–Ni 2/rGO	−25(2.2)	−35(1.5)	0.35(0.02)	50(1.4)
Au–Ni 3rGO	−7(1.1)	−33(1.2)	0.6(0.04)	40(1.2)
Pt/C	~0.0(0.04)	−31(0.3)	0.8(0.01)	35(0.07)

confirm the high HER kinetics of the Au–Ni/rGO catalysts. The catalyst Au–Ni 3/rGO with an overpotential of 40 mV, which is very near to that of Pt/C (35 mV), to obtain a high current density 10 mA cm^{-2} also represents a more efficient catalyst relative to other HER catalysts (Supplementary Table S3).

The HER inherent activity of our electrocatalysts was also assessed by their measured Tafel slope. The values of β_c recorded in Table 3 showed a marked decrease from 211 mV dec^{-1} for bare rGO to 77, 66, 40, 35, and 33 mV dec^{-1} for Au NPs/rGO, Ni NPs/rGO, Au–Ni 1/rGO, Au–Ni 2/rGO, and Au–Ni 3/rGO, respectively. This decrease in the β_c values indicates accelerated kinetics of the HER, as lower Tafel slopes refer to the increase in the number of accessible active sites [68,69]. The low Tafel slopes (35 and 33 mV dec^{-1}) measured for the two best catalysts are very close to that of Pt/C catalyst (31 mV dec^{-1}) and comparable to or lower than other efficient catalysts in the literature (Supplementary Table S3), thus signifying the superior HER kinetics of these materials.

The low Tafel slopes measured for Au–Ni/rGO catalysts, which are close to that of Pt, suggest that the rate limiting step is the recombination step [8,70,71]. These findings mean that the HER proceeds *via* a primary discharge step (Volmer reaction, $H_3O^+ + e^- = H_{ads} + H_2O$, with $\beta_c \sim 120$ mV), followed by a recombination step (Tafel reaction, $H_{ads} + H_{ads} = H_2$, with $\beta_c \sim 30$ mV) thus, the Volmer–Tafel mechanism is assumed to control the HER on the Au–Ni/rGO catalysts.

Turn over frequency (TOF), the number of hydrogen molecules that are formed per second per active site [72,73], was also used to assess the HER activity per site of a catalyst at a given overpotential. Values of TOF were calculated, as described elsewhere [74], at 200 mV using the BET surface areas measured for the tested catalysts. It is seen that TOF of the bare rGO increased significantly from 5.2×10^{-2} H_2/s per active site to 1.02, 1.63, 2.2, 2.8, and 3.3H_2/s per active site for Au NPs/rGO, Ni NPs/rGO, Au–Ni 1/rGO, Au–Ni 2/rGO, and Au–Ni 3/rGO, respectively. The obvious increase in TOF of the three Au–Ni/rGO catalysts with Ni content further confirms that the synergism in the Au–Ni nano-alloy is extremely helpful for the greatly enhanced HER electrocatalytic activity of the Au–Ni/rGO catalysts. The enhanced TOF values of the studied Au–Ni/rGO catalysts with Ni content are translated in increased Faradaic efficiency (*FE*), as shown in Table 4. Values of *FE* were calculated from the ratio of the experimentally measured volume of H_2 to its theoretical volume (more details are reported in the Supporting Information). Such volumes

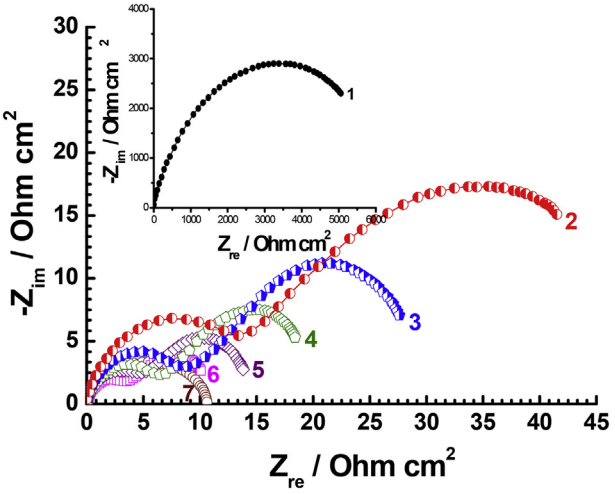

Fig. 5 – Complex-plane impedance plots recorded for the studied electrocatalysts loaded onto a glassy carbon electrode (rotation speed 1600 rpm). Measurements were conducted in deaerated H_2SO_4 aqueous solution (0.5 M) at a cathodic overpotential of −0.35 V *vs.* RHE at 25 °C: (1) bare rGO; (2) Au NPs/rGO; (3) Ni NPs/rGO; (4) Au–Ni 1/rGO; (5) Au–Ni 2/rGO; (6) Au–Ni 3/rGO; (7) Pt/C.

(measured and calculated) of H_2 recorded for the best catalyst (Au–Ni 3/rGO) as well as for the other studied catalysts and Pt/C are compared in Fig. S5 (SI) as a function of time (10–60 min).

The charge (*C*) – time (*t*) curves were also constructed for the studied catalysts in a comparison with Pt/C to gain more insight into their electrochemical efficiency for H_2 generation. Such plots, Fig. S6 (SI), were obtained during a controlled potential electrolysis process performed in 0.5 M H_2SO_4 solution, where the tested catalyst was held at −0.8 V *vs* RHE for 1 h. It follows from Fig. S6 that the *C*-*t* plot of the best catalyst (curve 5) is very close to that of Pt/C (curve 6). The measured volume of H_2 produced by this catalyst (19.1 μmol h^{-1}, with a corresponding *FE* of 99%) also approached that of Pt/C (19.5 μmol h^{-1}, *FE* ~ 100%). These findings confirm the superior catalytic activity of Au–Ni 3/rGO catalyst. The catalytic impact of Au–Ni alloy NPs' synergism, which enhances with Ni content, is also evident here. This is clear from Table 4, where the values of *FE* were calculated to be 91.1, 93.9, 95.1, 96.6, and 99% for Au/rGO, Ni/rGO, Au–Ni 1/rGO, Au–Ni 2/rGO, and Au–Ni 3/rGO, respectively.

Table 4 – Mean value (standard deviation) of the measured and calculated volumes of H_2 after 1 h of a controlled potential electrolysis process[a], together with the Faradaic Efficiency values, *FE* (%), for the studied catalysts.

Catalyst	H_2 measured by gas chromatography (H_2/μmol h^{-1})	Calculated H_2 based on the charge passed during electrolysis		
		Charge passed/C	H_2/μmol h^{-1}	FE (%)
Au NPs/rGO	13.3(0.24)	2.82(0.026)	14.6(0.14)	91.1(0.77)
Ni NPs/rGO	14.8(0.28)	3.04(0.028)	15.76(0.15)	93.9(0.88)
Au–Ni 1/rGO	15.6(0.3)	3.16(0.03)	16.4(0.16)	95.1(0.9)
Au–Ni 2/rGO	17(0.33)	3.4(0.04)	17.6(0.19)	96.6(0.83)
Au–Ni 3/rGO	18.9(0.36)	3.69(0.05)	19.1(0.2)	99(0.85)
Pt/C	19.4(0.38)	3.75(0.05)	19.44(0.22)	99.8(0.83)

[a] A potentiostatic experiment where the catalyst is held at −0.85 V vs RHE for 1 h in 0.5 M H_2SO_4 deaerated solution at 25 °C.

EIS measurements were also carried out at a given overpotential, −0.35 V *vs.* RHE, to further assess the HER kinetics over the studied catalysts. The Nyquist plots of the synthesized catalysts (Fig. 5, curves 2–6) are characterized by two well-defined depressed semicircles. The high frequency semicircle (with diameter R_1) was assigned to adsorbed hydrogen, while that formed at medium- and low frequency, whose diameter is R_2, was attributed to HER kinetics. The charge-transfer resistance (R_{ct}) associated with the whole process is given by the summation of R_1 and R_2 [34]. Bare rGO and Pt/C displayed a single capacitive loop, which can be assigned to a resistance-capacitance (*RC*) network. This network consists of a charge-transfer resistance due to the reduction of H^+ and the corresponding capacitance (*C*) [34].

The impedance data were fitted using the equivalent circuits presented in Fig. 6, and fully described elsewhere [34]. The obtained fitting parameters are listed in Table 5. It follows from Table 5 that our catalysts exhibited markedly reduced R_{ct} values (11–50 Ω cm^2) than that measured for the bare rGO (R_{ct} = 6770 Ω cm^2), demonstrating fast HER kinetics over their surfaces. The three synthesized Au–Ni alloy NPs/rGO catalysts exhibited the least R_{ct} values (23.6, 16.5, and 11.6 Ω cm^2 for Au–Ni 1/rGO, Au–Ni 2/rGO and Au–Ni 3/rGO, respectively), which diminish with increasing Ni concentration in the Au–Ni alloy NPs, among the studied catalysts (49.9 and 30.4 Ω cm^2 for Au NPs/rGO and Ni NPs/rGO, respectively). These results confirm the outstanding HER activity of such catalysts that arises from the synergism of Au and Ni in the loaded nano-alloy Au–Ni system. The low R_{ct} values of these materials refer to their increased conductivity, which improves the charge transfer characteristics of the loaded NPs. This in turn enhances electron transfer during the H^+ reduction process over their surfaces. Further inspection of Table 5 reveals that the R_{ct} value (11.6 Ω cm^2) of the best catalyst, namely Au–Ni 3/rGO, is very close to that of the Pt/C catalyst (10.6 Ω cm^2), thus confirming its superior HER activity. The capacitance (*C*) is proportional to the area of contact between the catalysts and the electrolyte; high contact area is favorable for high activity. For instance, the total capacitance value, $C_{total} = C_1 + C_2$, recorded for Ni NPs/rGO is 252.44 μF cm^{-2}, which is ~2.2 times greater than that measured for Au NPs/rGO (115.8 μF cm^{-2}) and 17 times larger in comparison to bare rGO (14.8 μF cm^{-2}). These findings are consistent with the BET surface areas in Table 1. However, Au–Ni/rGO catalysts, whose BET surface areas are lower than that of Ni NPs/rGO (Table 1), showed C_{total} values of 459.5, 822.7, and 965.1 μF cm^{-2} for Au–Ni 1/rGO, Au–Ni 2/rGO, and Au–Ni 3/rGO, respectively which increase with Ni content, much higher than that of Ni NPs/rGO (252.44 μF cm^{-2}). These findings again highlight the highly important role of the synergism in the loaded Au–Ni alloy NPs in enhancing HER activity of Au–Ni/rGO catalysts. The high HER activity of such materials is likely due to the abundance of active catalytic sites (the Au and Ni metallic nanoparticles loaded on the rGO nanosheets), the increased electrochemically accessible surface area, significantly improved electrochemical conductivity, and the synergism that exists between Au and Ni NPs in the Au–Ni nano-alloy.

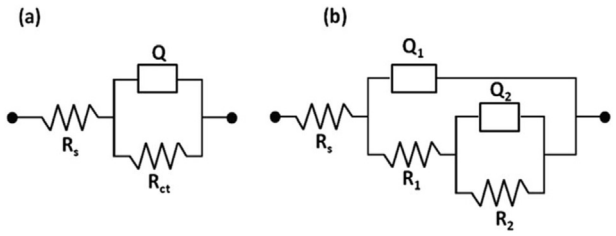

Fig. 6 – Equivalent circuits used to fit the experimental impedance data; (a) for Pt/C and bare rGO, (b) for the other tested catalysts.

Catalytic activity for the ORR

The promising HER kinetics (including a low onset potential of −7 mV, a Tafel slope as low as 33 mV dec^{-1}, a large j_o value of 0.6 mA cm^{-2}, and a TOF value of 3.3H_2/s per active site) recorded for the best catalyst here, namely Au–Ni 3/rGO, highlight its outstanding HER activity. This catalyst also achieved higher catalytic activity towards ORR in comparison to the other tested catalysts, where RDE measurements were employed to study the kinetics of the ORR over all the synthesized nanocomposite catalysts. Measurements were conducted in O_2-saturated aqueous H_2SO_4 solution (0.5 M) at a rotation speed of 1600 rpm and a scanning rate of 5 mV s^{-1}, Fig. 7a.

Like Pt/C, the value of E_{ORR} (the onset potential for O_2 reduction) recorded for Au–Ni 3/rGO catalyst is ~1.0 V vs. RHE, which is about 20, 40, 55, 90, and 360 mV more positive than that measured for Au–Ni 2/rGO, Au–Ni 1/rGO, Ni NPs/rGO, Au NPs/rGO, and bare rGO catalysts, respectively. The catalyst Au–Ni 3/rGO also exhibited the highest ORR limiting current density (4.4 mA cm^{-2} @ −0.5 V *vs.* RHE) among the tested catalysts, which is very close to that recorded for Pt/C (4.5 mA cm^{-2}) at the same potential. In addition, the Au–Ni 3/rGO achieved an ORR half-wave potential, $E_{1/2}$, of 0.9 V vs. RHE, which is very close to that of Pt/C, 0.91 V vs. RHE, and its corresponding ORR current density is the highest (~2.3 mA cm^{-2}; also very close to that measured for Pt/C, ~2.4 mA cm^{-2}), amongst the tested catalysts. This half-wave potential value is about 30, 70, 100, 140, and 410 mV more positive than that recorded for Au–Ni 2/rGO, Au–Ni 1/rGO, Ni NPs/rGO, Au NPs/rGO, and bare rGO catalysts, respectively. Based on the above findings, the ORR activity of our synthesized catalysts follows the same sequence of increased HER activity, namely Pt/C ~ Au–Ni 3/rGO > Au–Ni 2/rGO > Au–Ni 1/rGO > Ni NPs/rGO ≫ Au NPs/rGO.

Mechanism of ORR

Fig. 7b shows the cathodic polarization curves that are recorded for the most active catalyst in 0.5 M H_2SO_4 O_2-saturated aqueous solution as a function of the rotation speed (100–3600 rpm). This figure is constructed to determine the number of electrons that are transferred per O_2 molecule during ORR catalyzed by the best catalyst using the Koutecky-Levich equation [75,76]. It is obvious that, at potentials anodic to E_{ORR}, the ORR on the Au–Ni 3/rGO catalyst is under kinetic control; ORR insensitive to the rotation speed. The ORR is under mixed diffusion kinetic control at intermediate potentials. At less positive potentials, the reaction rate is controlled by mass transport, and a well-defined limiting current region

Table 5 – Mean value (standard deviation) of the impedance parameters recorded for the studied catalysts. Measurements were conducted in 0.5 M H_2SO_4 deaerated solutions at a cathodic potential of −0.35 V *vs* RHE at 25 °C.

Catalyst	Q_1 S^n (ω^{-1} cm^{-2})	R_1 Ω cm^2	n_1	C_1 μF cm^{-2}	Q_2 S^n (ω^{-1} cm^{-2})	R_2 Ω cm^2	n_2	C_2 μF cm^{-2}	R_{ct} Ω cm^2
Au NPs/rGO	194.4(1.7)	14.9(0.22)	0.87	81.2(1.6)	72.4(0.48)	35(0.6)	0.89	34.6(0.4)	49.9(0.82)
Ni NPs/rGO	324.5(3.2)	9.4(0.14)	0.89	158.6(2.8)	175(1.4)	21(0.4)	0.9	93.84(1.2)	30.4(0.54)
Au–Ni 1/rGO	458(4.8)	7.8(0.12)	0.9	244.8(4.6)	358.2(3.1)	15.8(0.3)	0.91	214.7(2.9)	23.6(0.42)
Au–Ni 2/rGO	778.6(8.6)	6.8(0.1)	0.9	434.9(8.2)	606(5.43)	9.7(0.19)	0.92	387.8(5.2)	16.5(0.29)
Au–Ni 3/rGO	860.6(10.2)	4.1(0.07)	0.92	526.7(9.7)	653.6(6.14)	7.5(0.15)	0.93	438.4(5.9)	11.6(0.22)

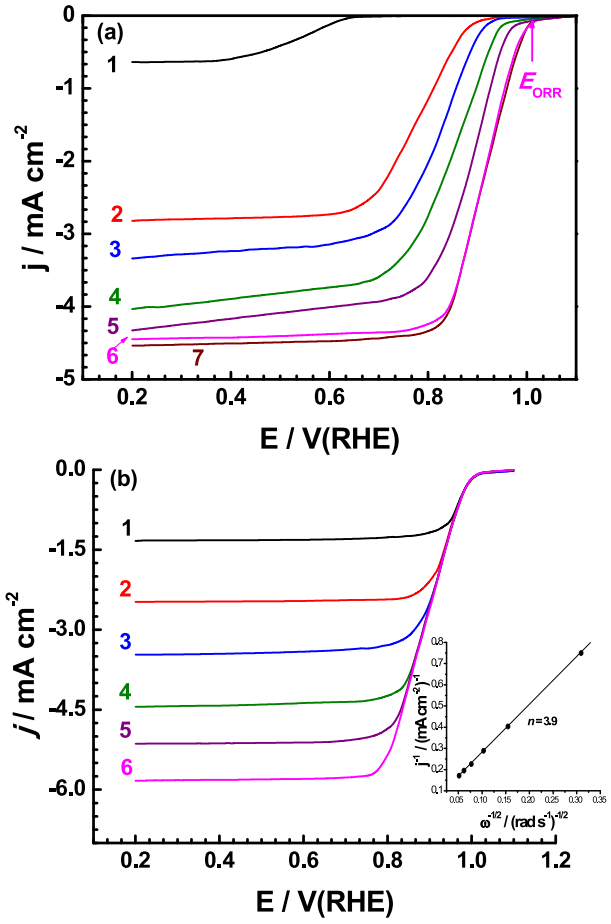

Fig. 7 – (a) Cathodic polarization curves recorded for the studied electrocatalysts loaded onto a glassy carbon electrode (rotation speed 1600 rpm). (b) Effect of rotation speed (100–3600 rpm) on the cathodic behavior of the best catalyst, Au–Ni 3/rGO. Inset of Fig. 7 (b): K-L relation for the best catalyst demonstrating the $4e^-$ mechanism of the ORR. Measurements were conducted in deaerated H_2SO_4 aqueous solution (0.5 M) at a scan rate of 5 mV s^{-1} at 25 °C. (1) bare rGO; (2) Au NPs/rGO; (3) Ni NPs/rGO; (4) Au–Ni 1/rGO; (5) Au–Ni 2/rGO; (6) Au–Ni 3/rGO; (7) Pt/C.

appears. As expected, the density of current increases with the rotation speed due to the enhancement in the mass transfer of O_2 [76]. The number of electrons that are transferred during the ORR process on the Au–Ni 3/rGO cathode is estimated to be 4 electrons per one O_2 molecule, see Koutecky-Levich plot in the inset of Fig. 7b. This result suggests that the ORR process catalyzed by this catalyst takes place *via* a four-electron pathway.

Long term stability and catalyst activation

Understanding the stability of electrocatalysts is a critical aspect in the development of this field [77]. For real working devices, repetitive stability tests in excess of 10,000 potential cycles are recommended [78]. For this reason, long-term potential cycling was carried out for the best catalyst, namely Au–Ni 3/rGO by recording continuous cyclic voltammograms at an accelerated scanning rate of 50 mV s^{-1} for 10,000 cycles, Fig. 8a, to assess its durability properly.

It is seen that the HER activity of the catalyst is markedly enhanced after 10,000 cycles, even at lower overpotentials, thus the catalyst is activated during the reaction. Activation of the catalyst during cathodic polarization of continuous potential cycles was reproducible in this work, and was also previously obtained [34,79]. At the end of the operation, the HER activity of the activated catalyst is found to surpass that of Pt/C (Tafel slope: 31 mV dec^{-1} and exchange current density: 0.8 mA cm^{-2}). This is clear from the Tafel plot of the 10,000th cycle that is shown in the inset of Fig. 8a, where a Tafel slope as low as 29.3 mV dec^{-1} and an exchange current density of 1.17 mA cm^{-2} were obtained. During this long stability testing, where hydrogen evolves progressively, the supported Au–Ni alloy NPs can adsorb hydrogen into their structure [80,81] even the substrate itself, namely rGO adsorbs hydrogen [82] and is found here to be activated during the run. This adsorbed hydrogen breaks down Au–Ni alloy NPs and rGO. This in turn increases the surface area of the catalyst and also creates new defect sites required for HER [34,79]. BET measurements also reveals that the specific surface area of the best catalyst has increased from 240.05 m^2/g before activation to 624.49 m^2/g after activation (i.e., at the end of the 10,000th cycle). Similar results were obtained for bare rGO, where its specific surface area has increased from 37.02 to 108.07 m^2/g after 10,000 cycles of cathodic polarization (revisit Table 1). These findings reveal the catalytic impact of the adsorbed hydrogen.

The practical operation of the best catalyst was also examined by electrolysis at a fixed cathodic overpotential (chronoamperometry measurements) up to 24 h, to further confirm catalyst durability and activation during the long term operation, Fig. 8b. Within the first 5 min of the run, the cathodic current density decreased quickly from −0.17 A cm^{-2} to −0.06 A cm^{-2}. This decrease in current denotes catalyst deactivation due to catalyst poisoning and/or H_2 bubble accumulation [83]. The catalytic current then declines over the 24 h of continuous operation due to H_2 release [83], thus

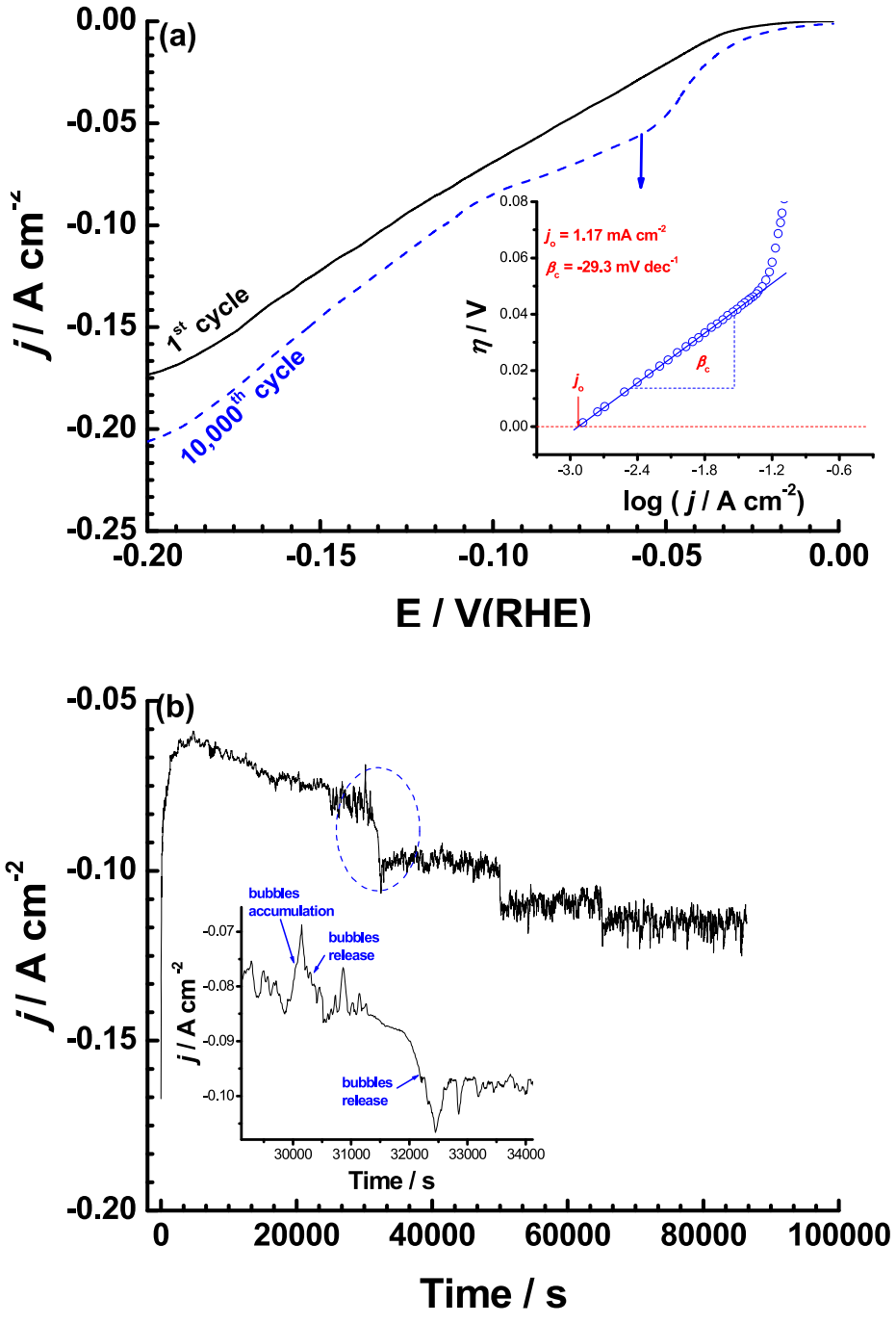

Fig. 8 – Material stability: (a) effect of repetitive cycling (10,000 cycles) between E_{corr} and −0.2 V *vs.* RHE at a scan rate of 50 mV s^{-1} on the HER activity of Au–Ni 3/rGO (the best catalyst) - Inset: fitting to the Tafel equation after the 10,000th cycle. (b) Chronoamperometry measurements (*j vs. t*) recorded on the best catalyst at a constant applied potential of −0.85 V *vs.* RHE. Measurements were performed in deaerated H_2SO_4 aqueous solution (0.5 M) at 25 °C.

showing an increased in the catalytic activity for the HER, to a reasonably steady value at ~ 0.12 A cm^{-2}. Such excellent durability and activation is highly promising for practical applications of the catalyst over long term operation.

Conclusion

Au–Ni alloy nanoparticles have been synthesized on reduced graphene oxide (rGO) sheets with three different ratios by a simple solution chemistry approach. The nanocomposites were characterized by high resolution transmission electron microscopy, X-ray photoelectron spectroscopy, diffuse reflectance infrared Fourier transform, X-ray diffraction, and thermal gravimetric analysis. The nanocomposites exhibited high electrocatalytic activity toward hydrogen evolution reaction (HER) and oxygen reduction reaction (ORR) in sulfuric acid aqueous solutions. The catalytic activity of the Ni NPs/rGO catalyst exceeded that of Au NPs/rGO, due to the smaller average particle size and the larger accessible electrochemical

active surface area of the former. The catalytic activity of the tested nanocomposites toward both reactions has significantly increased when Au and Ni NPs are brought together as bimetallic NPs on the rGO substrate. The activity of the Au–Ni alloy NPs/rGO catalysts are found to enhance markedly with increasing Ni concentration, approaching that of the commercial Pt/C catalyst. Synergism between Ni and Au in the loaded Au–Ni alloy NPs is proved to be the primary reason for the superior catalytic activity of Au–Ni alloy NPs/rGO catalysts. RDE experiments revealed superior electrocatalytic activity for the reduction of dissolved oxygen on Au–Ni alloy NPs/rGO catalysts with a four-electron mechanism, as evidenced from K-L plots.

Acknowledgements

The authors are thankful to the Director, CSIR–NEIST, Jorhat for his interest to carry out the work. GD gratefully acknowledges DST, India for DST-INSPIRE Fellowship. The authors further acknowledge SAIF, NEHU, Shillong for the HRTEM facility. S.S. and R.B. acknowledge financial support from the Centre National de la Recherche Scientifique (CNRS), the Lille University and the Hauts-de-France region.

Appendix A. Supplementary data

Supplementary data related to this article can be found at https://doi.org/10.1016/j.ijhydene.2017.11.048.

REFERENCES

[1] Morales-Guio CG, Stern LA, Hu X. Nanostructured hydrotreating catalysts for electrochemical hydrogen evolution. Chem Soc Rev 2014;43:6555–69.
[2] Rostrup-Nielsen JR. Fuels and energy for the future: the role of catalysis. Catal Rev Sci Eng 2004;46:247–70.
[3] Cook TR, Dogutan DK, Reece SY, Surendranath Y, Teets TS, Nocera DG. Solar energy supply and storage for the legacy and nonlegacy worlds. Chem Rev 2010;110:6474–502.
[4] Zhang Z, Lu B, Hao J, Yang W, Tang J. FeP nanoparticles grown on graphene sheets as highly active non-precious-metal electrocatalysts for hydrogen evolution reaction. Chem Commun 2014;50:11554–7.
[5] Fontecilla-Camps JC, Volbeda A, Cavazza C, Nicolet Y. Structure/function relationships of [NiFe]- and [FeFe]-Hydrogenases. Chem Rev 2007;107:4273–303.
[6] Thoi VS, Sun Y, Long JR, Chang CJ. Complexes of earth-abundant metals for catalytic electrochemical hydrogen generation under aqueous conditions. Chem Soc Rev 2013;42:2388–400.
[7] Huang X, Zeng Z, Bao S, Wang M, Qi X, Fan Z, et al. Solution-phase epitaxial growth of noble metal nanostructures on dispersible single-layer molybdenum disulfide nanosheets. Nat Commun 2013;4:1444–52.
[8] Xu Y, Zhang B. Recent advances in porous Pt-based nanostructures: synthesis and electrochemical applications. Chem Soc Rev 2014;43:2439–50.
[9] Esposito DV, Chen JG. Monolayer platinum supported on tungsten carbides as low-cost electrocatalysts: opportunities and limitations. Energy Environ Sci 2011;4:3900–12.
[10] Roy N, Leung KT, Pradhan D. Nitrogen doped reduced graphene oxide based Pt-TiO_2 nanocomposites for enhanced hydrogen evolution. J Phys Chem C 2015;119:19117–25.
[11] Esposito DV, Hunt ST, Kimmel YC, Chen JG. A new class of electrocatalysts for hydrogen production from water electrolysis: metal monolayers supported on low-cost transition metal carbides. J Am Chem Soc 2012;134:3025–33.
[12] Luo P, Jiang L, Zhang W, Guan X. Graphene quantum Dots/Au hybrid nanoparticles as electrocatalyst for hydrogen evolution reaction. Chem Phys Lett 2015;641:29–32.
[13] Sai Siddhardha RS, Lakshminarayanan V, Ramamurthy SS. Spot-free Catalysis Using Gold Carbon Nanotube & Gold Graphene Composites for hydrogen evolution reaction. J Power Sources 2015;288:441–50.
[14] Huff C, Dushatinski T, Abdel-Fattah TM. Gold nanoparticle/multi-walled carbon nanotube composite as novel catalyst for hydrogen evolution reactions. Int J Hydrogen Energy 2017;42:18985–90.
[15] Yang Q, Dong M, Song H, Cao L, Zhang Y, Wang L, et al. Size dependence electrocatalytic activity of gold nanoparticles decorated reduced graphene oxide for hydrogen evolution reaction. J Mater Sci Mater Electron 2017;28:10073–80.
[16] Govindhan M, Chen A. Simultaneous synthesis of gold nanoparticle/graphene nanocomposite for enhanced oxygen reduction reaction. J Power Sources 2015;274:928–36.
[17] Jiang L, Hsu A, Chu D, Chen R. Size-dependent activity of palladium nanoparticles for oxygen electroreduction in alkaline solutions. J Electrochem Soc 2009;156:B643–9.
[18] Jukk K, Alexeyeva N, Ritslaid P, Kozlova J, Sammelselg V, Tammeveski K. Electrochemical reduction of oxygen on heat-treated Pd nanoparticle/multi-walled carbon nanotube composites in alkaline solution. Electrocatalysis 2013;4:42–8.
[19] Jukk K, Kongi N, Matisen L, Kallio T, Kontturi K, Tammeveski K. Electroreduction of oxygen on palladium nanoparticles supported on nitrogen-doped graphene nanosheets. Electrochim Acta 2014;137:206–12.
[20] Liu S, Zhang Q, Li Y, Han M, Gu L, Nan C, et al. Five-fold twinned Pd_2NiAg nanocrystals with increased surface Ni site availability to improve oxygen reduction activity. J Am Chem Soc 2015;137:2820–3.
[21] Chakrabartty S, Gopinath CS, Retna Raj C. Polymer-based hybrid catalyst of low Pt content for electrochemical hydrogen evolution. Int J Hydrogen Energy 2017;42:22821–9.
[22] Jiao F, Frei H. Nanostructured cobalt and manganese oxide clusters as efficient water oxidation catalysts. Energy Environ Sci 2010;3:1018–27.
[23] Merki D, Hu X. Recent developments of molybdenum and tungsten sulfides as hydrogen evolution catalysts. Energy Environ Sci 2011;4:3878–88.
[24] Padmapriya S, Harinipriya S, Sudha V, Kumar D, Pal S, Chaubey B. Polyaniline coated copper for hydrogen storage and evolution in alkaline medium. Int J Hydrogen Energy 2017;42:20453–62.
[25] Chen W-F, Sasaki K, Ma C, Frenkel AI, Marinkovic NJ, Muckerman T, et al. Hydrogen-evolution catalysts based on non-noble metal nickel-molybdenum nitride nanosheets. Angew Chem Int Ed 2012;51:6131–5.
[26] Hsu IJ, Kimmel YC, Jiang X, Willis BG, Chen JG. Atomic layer deposition synthesis of platinum-tungsten carbide core-shell catalysts for the hydrogen evolution reaction. Chem Commun 2012;48:1063–5.
[27] Kong D, Wang H, Lu Z, Cui Y. $CoSe_2$ nanoparticles grown on carbon fiber paper: an efficient and stable electrocatalyst for hydrogen evolution reaction. J Am Chem Soc 2014;136:4897–900.

[28] Zhang J, Zhu Z, Tang Y, Muellen K, Feng X. Titania nanosheet-mediated construction of a two-dimensional titania/cadmium sulfide heterostructure for high hydrogen evolution activity. Adv Mater 2014;26:734–8.
[29] Xu H, Yan B, Zhang K, Wang J, Li S, Wang C, et al. Ultrasonic-assisted synthesis of N-doped graphene-supported binary PdAu nanoflowers for enhanced electro-oxidation of ethylene glycol and glycerol. Electrochim Acta 2017;245:227–36.
[30] Xu H, Zhang K, Yan B, Wang J, Wang C, Li S, et al. Ultra-uniform PdBi nanodots with high activity towards formic acid oxidation. J Power Sources 2017;356:27–35.
[31] Xu H, Yan B, Wang J, Zhang K, Li S, Xiong Z, et al. Self-supported porous 2D AuCu triangular nanoprisms as model electrocatalysts for ethylene glycol and glycerol oxidation. J Mater Chem A 2017;5:15932–9.
[32] Xu H, Wang J, Yan B, Zhang K, Li S, Wang C, et al. Hollow Au_xAg/Au core/shell nanospheres as efficient catalysts for electrooxidation of liquid fuels. Nanoscale 2017;9:12996–3003.
[33] Greeley J, Jaramillo TF, Bonde J, Chorkendorff I, Norskov JK. Computational high-throughput screening of electrocatalytic materials for hydrogen evolution. Nat Mater 2006;5:909–13.
[34] Darabdhara G, Amin MA, Mersal GAM, Ahmed EM, Das MR, Zakaria MB, et al. Reduced graphene oxide nanosheets decorated with Au, Pd and Au-Pd bimetallic nanoparticles as highly efficient catalysts for electrochemical hydrogen generation. J Mater Chem A 2015;3:20254–66.
[35] Totha PS, Velicky M, Slater TJA, Worrall SD, Haigh SJ. Hydrogen evolution and capacitance behavior of Au/Pd nanoparticle-decorated graphene heterostructures. Appl Mater Today 2017;8:125–31.
[36] Mandegarzad S, Raoof JB, Hosseini SR, Ojani R. Cu-Pt bimetallic nanoparticles supported metal organic framework-derived nanoporous carbon as a catalyst for hydrogen evolution reaction. Electrochim Acta 2016;190:729–36.
[37] Wang L, Qi B, Sun L, Sun Y, Guo C, Li Z. Synthesis and assembly of Au-Pt bimetallic nanoparticles. Mater Lett 2008;62:1279–82.
[38] Raoof J-B, Ojani R, Rashid-Nadimi S. Electrochemical synthesis of bimetallic Au@Pt nanoparticles supported on gold film electrode by means of self-assembled monolayer. J Electroanal Chem 2010;641:71–7.
[39] Chen Y-L, Xiong L, Song X-N, Wang W-K, Huang Y-X, Yu H-Q. Electrocatalytic hydrodehalogenation of atrazine in aqueous solution by Cu@Pd/Ti catalyst. Chemosphere 2015;125:57–63.
[40] Li SS, Wang AJ, Hu YY, Fang KM, Chen JR, Feng JJ. One-step, seedless wet-chemical synthesis of gold@palladium nanoflowers supported on reduced graphene oxide with enhanced electrocatalytic properties. J Mater Chem A 2014;2:18177–83.
[41] Ma X, Zhao K, Tang H, Chen Y, Lu C, Liu W, et al. New insight into the role of gold nanoparticles in Au@CdS core–shell nanostructures for hydrogen evolution. Small 2014;10:4664–70.
[42] Lang L, Shi Y, Wang J, Wang F-B, Xia X-H. Hollow core-shell structured Ni-Sn@C nanoparticles: a novel electrocatalyst for the hydrogen evolution reaction. ACS Appl Mater Interfaces 2015;7:9098–102.
[43] Huber GW, Shabaker JW, Dumesic JA. Raney Ni-Sn catalyst for H_2 production from biomass-derived hydrocarbons. Science 2003;300:2075–7.
[44] Krstajic NV, Jovic VD, Gajic-Krstajic L, Jovic BM, Antozzi AL, Martelli GN. Electrodeposition of Ni-Mo alloy coatings and their characterization as cathodes for hydrogen evolution in sodium hydroxide solution. Int J Hydrogen Energy 2008;33:3676–87.
[45] Gong M, Li Y, Wang H, Liang Y, Wu JZ, Zhou J, et al. An advanced Ni-Fe layered double hydroxide electrocatalyst for water oxidation. J Am Chem Soc 2013;135:8452–5.
[46] Gao M-R, Lin Z-Y, Zhuang T-T, Jiang J, Xu Y-F, Zheng Y-R, et al. Mixed-solution synthesis of sea urchin-like NiSe nanofiber assemblies as economical Pt-free catalysts for electrochemical H_2 production. J Mater Chem 2012;22:13662–8.
[47] McKone JR, Sadtler BF, Werlang CA, Lewis NS, Gray HB. Ni-Mo nanopowders for efficient electrochemical hydrogen evolution. ACS Catal 2013;3:166–9.
[48] Deng J, Ren P, Deng D, Bao X. Enhanced electron penetration through an ultrathin graphene layer for highly efficient catalysis of the hydrogen evolution reaction. Angew Chem Int Ed 2015;54:2100–4.
[49] Kuttiyiel KA, Sasaki K, Chen W-F, Su D, Adzic RR. Core-shell, hollow-structured iridium-nickel nitride nanoparticles for the hydrogen evolution reaction. J Mater Chem A 2014;2:591–4.
[50] Wang S, Yang G, Yang S. Pt-Frame@Ni quasi core-shell concave octahedral PtNi3 bimetallic nanocrystals for electrocatalytic methanol oxidation and hydrogen evolution. J Phys Chem C 2015;119:27938–45.
[51] Li J, Zhou P, Li F, Ren R, Liu Y, Niu J, et al. Ni@Pd/PEI-rGO stack sructures with controllable Pd shell thickness as advanced electrodes for efficient hydrogen evolution. J Mater Chem A 2015;3:11261–8.
[52] Liu M, Zhang R, Chen W. Graphene-supported nanoelectrocatalysts for fuel cells: synthesis, properties, and applications. Chem Rev 2014;114:5117–60.
[53] Wang QJ, Che JG. Origins of distinctly different behaviors of Pd and Pt contacts on graphene. Phys Rev Lett 2009;103:066802.
[54] Hummers WS, Offeman JRE. Preparation of graphitic oxide. J Am Chem Soc 1958;80:1339.
[55] Xiao F, Yang L, Zhao F, Zeng B. Electrodeposition of AuNi alloy nanoparticles on mercapto ionic liquid–graphite composite film and the amperometric determination of hydroquinone. Anal Bioanal Electrochem 2013;5:154–65.
[56] Chiang I-C, Chen Y-T, Chen D-H. Synthesis of NiAu colloidal nanocrystals with kinetically tunable properties. J Alloys Compds 2009;468:237–45.
[57] Chiu H-K, Chiang I-C, Chen D-H. Synthesis of NiAu alloy and core–shell nanoparticles in water-in-oil microemulsions. J Nanopart Res 2009;11:1137–44.
[58] Lv H, Xi Z, Chen Z, Guo S, Yu Y, Zhu W, et al. A new core/shell NiAu/Au nanoparticle catalyst with Pt-like activity for hydrogen evolution reaction. J Am Chem Soc 2015;137:5859–62.
[59] Das MR, Sarma RK, Borah SC, Kumari R, Saikia R, Deshmukh AB, et al. The synthesis of citrate-modified silver nanoparticles in an aqueous suspension of graphene oxide sheets and their antibacterial activity. Colloids Surf B 2013;105:128–36.
[60] Darabdhara G, Boruah PK, Borthakur P, Hussain N, Das MR, Ahamad T, et al. Reduced graphene oxide nanosheets decorated with Au–Pd bimetallic alloy nanoparticles towards efficient photocatalytic degradation of phenolic compounds in water. Nanoscale 2016;8:8276–87.
[61] Sharma P, Darabdhara G, Reddy TM, Borah A, Bezboruah P, Gogoi P, et al. Synthesis, characterization and catalytic application of Au NPs-reduced graphene oxide composites material: an eco-friendly approach. Catal Commun 2013;40:139–44.
[62] Darabdhara G, Sharma B, Das MR, Boukherroub R, Szunerits S. Cu-Ag bimetallic nanoparticles on reduced graphene oxide nanosheets as peroxidase mimic for glucose

and ascorbic acid detection. Sens Actuators B 2017;238:842–51.
[63] Grosvenor AP, Biesinger MC, Smart RSC, McIntyre NS. New interpretations of XPS spectra of nickel metal and oxides. Surf Sci 2006;600:1771–9.
[64] Oswald S, Brueckner W. XPS depth profile analysis of non-stoichiometric NiO films. Surf Interface Anal 2004;36:17–22.
[65] Peck MA, Langell MA. Comparison of nanoscaled and bulk NiO structural and environmental characteristics by XRD, XAFS, and XPS. Chem Mater 2012;24:4483–90.
[66] Abbaspour A, Norouz-Sarvestani F. High electrocatalytic effect of Au-Pd alloy nanoparticles electrodeposited on microwave assisted sol-gel-derived carbon ceramic electrode for hydrogen evolution reaction. Int J Hydrogen Energy 2013;38:1883–91.
[67] Lu Q, Hutchings GS, Yu W, Zhou Y, Forest RV, Tao R, et al. Highly porous non-precious bimetallic electrocatalysts for efficient hydrogen evolution. Nat Commun 2015;6:6567.
[68] Li J-S, Wang Y, Liu C-H, Li S-L, Wang Y-G, Dong L-Z, et al. Coupled molybdenum carbide and reduced graphene oxide electrocatalysts for efficient hydrogen evolution. Nat Commun 2016;7:11204.
[69] Candelaria SL, Shao Y, Zhou W, Li X, Xiao J, Zhang J-G, et al. Nanostructured carbon for energy storage and conversion. Nano Energy 2012;1:195–220.
[70] Sun Y, Liu C, Grauer DC, Yano J, Long JR, Yang P, et al. Electrodeposited cobalt-sulfide catalyst for electrochemical and photoelectrochemical hydrogen generation from water. J Am Chem Soc 2013;135:17699–702.
[71] Tran PD, Nguyen M, Pramana SS, Bhattacharjee A, Chiam SY, Fize J, et al. Copper molybdenum sulfide: a new efficient electrocatalyst for hydrogen production from water. Energy Environ Sci 2012;5:8912–6.
[72] Kibsgaard J, Jaramillo TF. Molybdenum phosphosulfide: an active, acid-stable, earth-abundant catalyst for the hydrogen evolution reaction. Angew Chem Int Ed 2014;53:14433–7.
[73] Kibsgaard J, Chen Z, Reinecke BN, Jaramillo TF. Engineering the surface structure of MoS_2 to preferentially expose active edge sites for electrocatalysis. Nat Mater 2012;11:963–9.
[74] Amin MA, Mostafa NY, Amin MA, Abd E-RSS, Ahmed EM, Alotibi MM, et al. Aluminum titania nanoparticle composites as nonprecious catalysts for efficient electrochemical generation of H_2. ACS Appl Mater Interfaces 2016;8:23655–67.
[75] Ahmed MS, Jeon S. The nanostructure of nitrogen atom linked carbon nanotubes with platinum employed to the electrocatalytic oxygen reduction. J Nanosci Nanotechnol 2013;13:306–14.
[76] Zhou R, Zheng Y, Jaroniec M, Qiao S-Z. Determination of the electron transfer number for the oxygen reduction reaction: from theory to experiment. ACS Catal 2016;6:4720–8.
[77] Fan X, Peng Z, Wang J, Ye R, Zhou H, Guo X. Carbon-based composite as an efficient and stable metal-free electrocatalyst. Adv Funct Mater 2016;26:3621–9.
[78] Markovic NM, Grgur BN. P.N. Ross, Temperature-dependent hydrogen electrochemistry on platinum low-index single-crystal surfaces in acid solutions. J Phys Chem B 1997;101:5405–13.
[79] Amin MA, Fadlallah SA, Alosaimi GS, Kandemirli F, Saracoglu M, Szunerits S, et al. Cathodic activation of titanium-supported gold nanoparticles: an efficient and stable electrocatalyst for the hydrogen evolution reaction. Int J Hydrogen Energy 2016;41:6326–41.
[80] Wang X, Sun S, Huang Z, Zhang H, Zhang S. Preparation and catalytic activity of PVP-protected Au/Ni bimetallic nanoparticles for hydrogen generation from hydrolysis of basic NaBH4 solution. Int J Hydrogen Energy 2014;39:905–16.
[81] Zaleska-Medynska A, Marchelek M, Diak M, Grabowska E. Noble metal-based bimetallic nanoparticles: the effect of the structure on the optical, catalytic and photocatalytic properties. Adv Colloid Interface Sci 2016;229:80–107.
[82] Venkatesan A, Patel RN, Kannan ES. Reduced graphene oxide for room temperature hydrogen storage application. Adv Mater Res 2015;1086:91–5.
[83] Xie J, Zhang H, Li S, Wang R, Sun X, Zhou M, et al. Defect-rich MoS_2 ultrathin nanosheets with additional active edge sites for enhanced electrocatalytic hydrogen evolution. Adv Mater 2013;25:5807–13.